

Influence of Grain Refinement on Microstructure and Mechanical Properties of Tungsten Carbide/Zirconia Nanocomposites

Ali Nasser, Mohamed A. Kassem, Ayman Elsayed, Mohamed A. Gepreel, and Ahmed A. Moniem

(Submitted September 4, 2015; in revised form August 17, 2016; published online September 21, 2016)

WC-W₂C/ZrO₂ nanocomposites were synthesized by pressure-less sintering (PS) and spark plasma sintering (SPS) of tungsten carbide/yttria-stabilized tetragonal zirconia, WC/TZ-3Y. Prior to sintering, WC/TZ-3Y powders were totally ball-milled for 20 and 120 h to obtain targeted nano (N) and nano-nano (N-N) structures, indicated by transmission electron microscopy and powder x-ray diffraction (PXRD). The milled powders were processed via PS at temperatures of 1773 and 1973 K for 70 min and SPS at 1773 K for 10 min. PXRD as well as SEM-EDS indicated the formation of WC-W₂C/ZrO₂ composites after sintering. The mechanical properties were characterized via Vicker microhardness and nanoindentation techniques indicating enhancements for sufficiently consolidated composites with high W₂C content. The effects of reducing particle sizes on phase transformation, microstructure and mechanical properties are reported. In general, the composites based on the N structure showed higher microhardness than those for N-N structure, except for the samples PS-sintered at 1773 K. For instance, after SPS at 1773 K, the N structure showed a microhardness of 18.24 GPa. Nanoindentation measurements revealed that nanoscale hardness up to 22.33 and 25.34 GPa and modulus of elasticity up to 340 and 560 GPa can be obtained for WC-W₂C/ZrO₂ nanocomposites synthesized by the low-cost PS at 1973 K and by SPS at 1773 K, respectively.

Keywords ceramics matrix, composites, mechanical properties, microhardness, nanoprocessing, sintering

1. Introduction

Cutting tools are typically produced from hard materials that can resist friction actions with maintained stability at elevated temperatures (Ref 1-3). In principle, tungsten carbide (WC) is a good candidate for cutting tools, drilling equipment and hardfacing applications due to its high hardness, moderate fracture toughness and high wear resistance at a wide range of temperatures (Ref 4-7). Because of its brittle nature, WC is usually prepared by adding a metal or metal oxide binder (Ref 5, 7-11). However, the low melting point of the metal and possibility of oxidation make the selection of the metal oxides binders more favorable for consolidating WC powders and improving its fracture toughness (Ref 12). Among all metal

oxides binders reported so far, tetragonal zirconia stabilized by 3 mol.% yttria provides WC-based composite (WC/TZ-3Y) with optimal mechanical and tribological properties needed for cutting tools applications (Ref 13-15). Recently, spark plasma sintering (SPS) and pressure-less sintering (PS) techniques have been proposed to consolidate WC/TZ-3Y composites and enhance its mechanical properties (Ref 4, 7, 15). Relatively, the SPS process introduces much higher heating rate, lower sintering temperature, T_s , and short heating cycle that maintain the nanosize and the submicron size of ZrO₂ and WC particles in the nanostructured WC/ZrO₂ composite (Ref 16-19). Regardless of the processing route, SPS or PS, WC/ZrO₂ composite shows superior hardness compared to other WC composites such as WC/Co (Ref 17, 20).

In general, reducing the powder particles and/or grains size down to the nanorange is required to improve the consolidation and mechanical properties especially for ceramics produced without applying hot pressing or field activated sintering, i.e., the classical PS technique (Ref 21). However, few reports have addressed the effect of nanoscopic structure of powder precursors on the mechanical properties of WC/TZ-3Y composites obtained at low and high T_s using PS and SPS techniques (Ref 15, 17, 22).

Based on the W-C phase diagram, WC and W₂C are stable phases, while α -WC_{1-x} is a metastable phase (Ref 23). The WC-W₂C composite grows by the thermodynamic equilibrium reaction of W and C at $T_s \geq 2653$ K in W concentration range of 50-76.6 at.%. However, non-equilibrium plasma melting of powder mixtures of WC and C with keeping the required W/C atomic ratio also results in the formation of WC-W₂C composite (Ref 24). Moreover, when WC undergoes a solidification or casting process in industry, it grows along with W₂C to produce a composite of WC + W₂C which is

Ali Nasser and Mohamed A. Gepreel, Materials Science and Engineering Department, Egypt-Japan University of Science and Technology, P.O. Box 179, New Borg El Arab City, Alexandria 21934, Egypt; Mohamed A. Kassem, Department of Materials Science and Engineering, Kyoto University, Kyoto 606-8501, Japan and Department of Physics, Assiut University, Assiut 71515, Egypt; Ayman Elsayed, Powder Technology Department, Central Metallurgical R&D Institute, Cairo 11421, Egypt; Ahmed A. Moniem, Materials Science and Engineering Department, Egypt-Japan University of Science and Technology, P.O. Box 179, New Borg El Arab City, Alexandria 21934, Egypt; and Physical Chemistry Department, National Research Center (NRC), Dokki, Cairo 12622, Egypt. Contact e-mails: kassem.ahmed.82s@st.kyoto-u.ac.jp and makassem@aun.edu.eg.

commercially known as the fused tungsten carbide (Ref 25, 26). The W_2C phase was also found to grow as a second phase with WC in a composite of WC with nanocrystalline ZrO_2 binder after SPS at $T \geq 1773$ K (Ref 22). Practically, higher performance of WC- W_2C composite than pure WC has been reported for applications of rock cutting and hardfacing applications due to its enhanced mechanical properties (Ref 24).

For exploring the particle size effects, two composites of WC/TZ-3Y with different structures were developed in the current study via excessive mechanical milling technique: (1) structure contains a mixture of submicron WC and nano-TZ-3Y particles, assigned hereafter as N composite; (2) structure contains a mixture of WC and TZ-3Y nanoparticles, assigned hereafter as N-N composites. The samples were post-sintered using PS and SPS techniques. Particular attention was given to the effects of these nanoscopic structures as well as T_s on the phase stability and mechanical properties of the consolidated WC/TZ-3Y composites at the microscale using Vickers microhardness and at the nanoscale using the nanoindentation.

2. Experimental Procedure

Commercially available WC (purity of 99.0%, 950 nm average particle size, KANTO CHEMICAL COMPANY-JAPAN) was used as a primary bulk phase, while ZrO_2 (purity of 99.0%, 20 μm average particle size) and Y_2O_3 (4N), KANTO CHEMICAL COMPANY-JAPAN, were used to prepare ZrO_2 -3 mol.% Y_2O_3 (TZ-3Y) as the binding phase. WC powder was first milled for 14 and 60 h in a RETCH PM 400 planetary ball milling machine to reach the submicron and the nanosizes, respectively. The TZ-3Y powder was milled separately for 60 h to obtain a very fine form of the binding phase. Rotating speed of 250 RPM in a 3-mm-diameter ZrO_2 balls as a grinding medium with a ball-to-powder weight ratio of 10:1 was used. Powders of the submicron and nano-WC were separately mixed with the fine TZ-3Y in a ratio of WC/TZ-3Y of 94:6 (wt.%) in a subsequent milling that lasted for 6 and 60 h to obtain the N and N-N composites, respectively. The milled powders were dried in a vacuum oven at 363 K for 19 h to remove trapped gases. The successive milling times for both composites are listed in Table 1.

The milled powder phases were characterized by powder x-ray diffraction (PXRD) using an x-ray diffractometer (LabX-PXRD-6100 Shimadzu) with CuK_{α} radiation ($\lambda = 0.154$ nm). The average grain size of each phase was estimated from the PXRD patterns using the Scherer's equation. Furthermore, microscopic investigations of the starting powders morphology, particle size and phase composition were performed using transmission electron microscopy (TEM) and its installed energy-dispersive x-ray spectroscopy (TEM-EDS). Consequently, high-resolution TEM, HRTEM, micrographs and

selected areas diffraction patterns, SADP, of the milled WC/TZ-3Y were obtained and indexed. All TEM investigations are performed using JEM-HR-2100 TEM.

PS and SPS techniques were employed to consolidate the N and N-N composites in desired densities closed to the theoretical density (TD). Prior to the PS, powder portions were uniaxially pressed to a relative density of $\sim 35\%$ TD in a 13-mm-cylindrical-steel die. The green compacted pellets were subjected to two different PS programs; the first program was carried out under vacuum at T_s of 1773 K for 70 min in a 0.10 MPa vacuumed furnace (GCA Vacuum Industries, Inc.), while the second was carried out at 1973 K for 70 min in a controlled argon atmosphere using $MoSi_2$ tube Furnace (Crystal Systems Co. Ltd.). Moreover, powders were charged directly without previous compaction in a 10-mm-diameter graphite die and sintered at 1773 K using SPS technique. SPS was conducted in a vacuum of 50-60 m torr (6.6-7.9 Pa) under a uniaxial pressure of 30 MPa. A high current of 1-1.2 kA was applied during the experiment to obtain a high heating rate up to 873 K/min. After a holding time of 10 min, the pressure was released.

The density of the consolidated composites was measured in distilled water according to the Archimedes' principle. Microstructural investigations were carried out for well-polished samples using Quanta FEG 250 scanning electron microscope (SEM). The resultant phases of the sintered composites were investigated by PXRD and SEM-EDS.

The mechanical properties of the consolidated samples were investigated using Shimadzu microhardness tester with force of 9.807 N applied for 10 s. The modulus of elasticity and nanoscale hardness were measured for N-N-structured specimens using the nanoindentation technique (Nano Test Vantage Apparatus) with low-load diamond indenter type (MT Perko- vetch-14406c). A load was applied in the range of 0.0001-0.1 N, and at least eight to ten readings of the hardness and Young's modulus were averaged for each data point.

3. Results and Discussion

3.1 Mechanical Milling and Sintering

Figure 1 shows TEM images for as-prepared WC/TZ-3Y powder (a) and N composites after 20-h milling (b). Typically, the particle size of both matrix and binding phases of WC/TZ-3Y powder was significantly reduced from microscale to nanoscale with milling. As seen, the TEM image of the N composite shows an average particle size for WC, dark particles indicated by red arrows, and TZ-3Y, indicated by blue arrows, phases of about 200 and 50 nm, respectively. It has also to be noted that the particles of TZ-3Y phase are homogeneously distributed around the surface of the WC matrix phase, which is

Table 1 Milling times and crystallites size, estimated from the PXRD patterns, for WC/TZ-3Y composites based on N and N-N structures

Powder	Milling time (h)			Crystallite size d_{XRD} (nm)	
	WC	TZ-3Y	WC/TZ-3Y	WC	TZ-3Y
Nanocomposite (N)	14	60	6	26	17
Nano-nano composite (N-N)	60	60	60	16	10

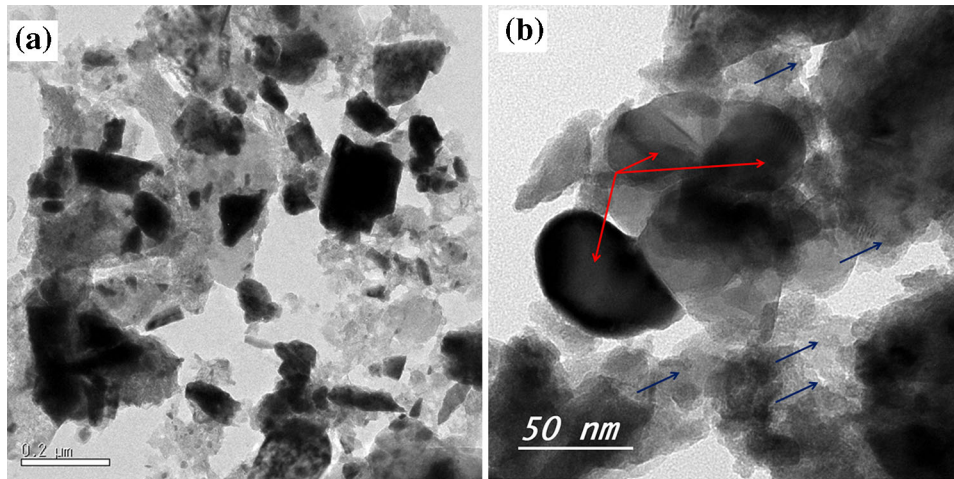


Fig. 1 (a) TEM micrograph for WC/TZ-3Y powders with slight mixing (before milling) showing bulk WC and TZ-3Y nanoparticles. (b) TEM image for a ball-milled WC/TZ-3Y powder for 20 h indicating submicron WC particles, indicated by red arrows, and nano-TZ-3Y particles, indicated by blue arrows (N structure)

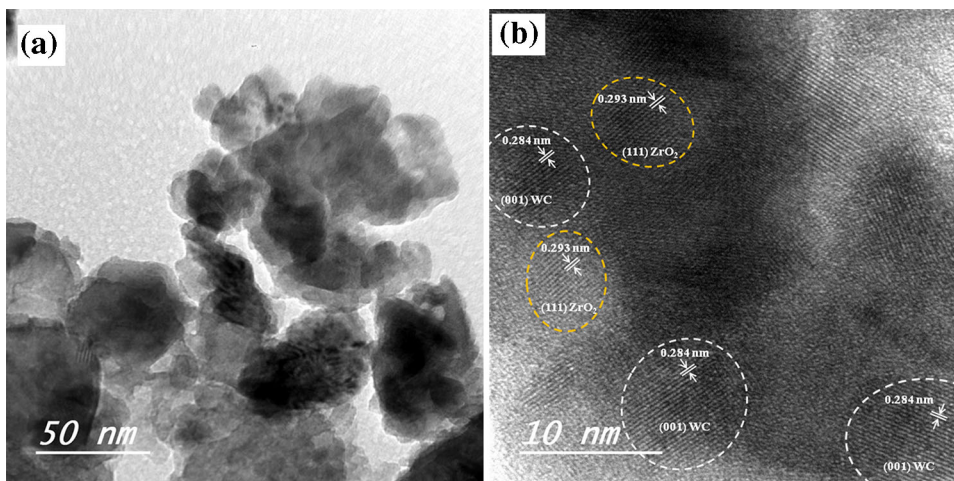


Fig. 2 (a) TEM image of WC/TZ-3Y composite after excessive mechanical milling for 120 h indicating the nanoparticle size of both WC and TZ-3Y (N-N structure). (b) High-resolution TEM (HRTEM) image showing the nanocrystalline structure of the N-N composite. The Moiré-like fringes indicate inter-planar distances corresponding to the (001) plane of WC and (111) plane of ZrO_2

typically the description of the nanostructured composite in the literature (Ref 27).

Meanwhile excessive milling for 120 h, N-N composite, leads to further reduction in particles size of both matrix and binding phases down to about 50 nm, as seen in a TEM image for N-N composite shown in Fig. 2(a). It is also worth noting that the particles of TZ-3Y phase seem to be partially agglomerated as a result of the excessive milling and the subsequent reduction of matrix phase particle size. However the uniformity of particles distribution is still maintained inside the structure. Furthermore, investigation of the ultra-fine nanocrystalline structure of N-N composite powder was performed by HRTEM. Figure 2(b) shows a HRTEM image of an intersection area between particles of N-N composite. Each particle contains many nanograins as indicated by the observed Moiré-like fringes. The Moiré-like fringes presented in the figure are indexed based on the inter-planar distances corresponding to

the projected planes. The dominant inter-planar distance of WC is 0.284 nm corresponding to the (001) plane, while for ZrO_2 , it is 0.293 nm corresponding to (111) plane. It was found that the grains of ZrO_2 are little smaller than those of WC and average sizes of both are close to 10 nm.

Further, accurate qualitative phase analysis was performed through the SADP which is able to detect phases of relative atomic ratios less than 0.1%. Figure 3(a) shows another TEM image for the N-N composite with indexed SADP shown in the insets. The selected areas are indicated as A and B corresponding to insets A and B of Fig. 3(a), respectively. The extra milling time for the N-N composite in a zirconia milling media resulted in extra zirconia content as indicated by the TEM-EDS spectrum and the element mappings shown in Fig. 3(b)-(g). TEM investigations clarified the effect of excessive milling process on the further reduction in particle and grain size. Fine particles of the N-N composite are expected to enhance the

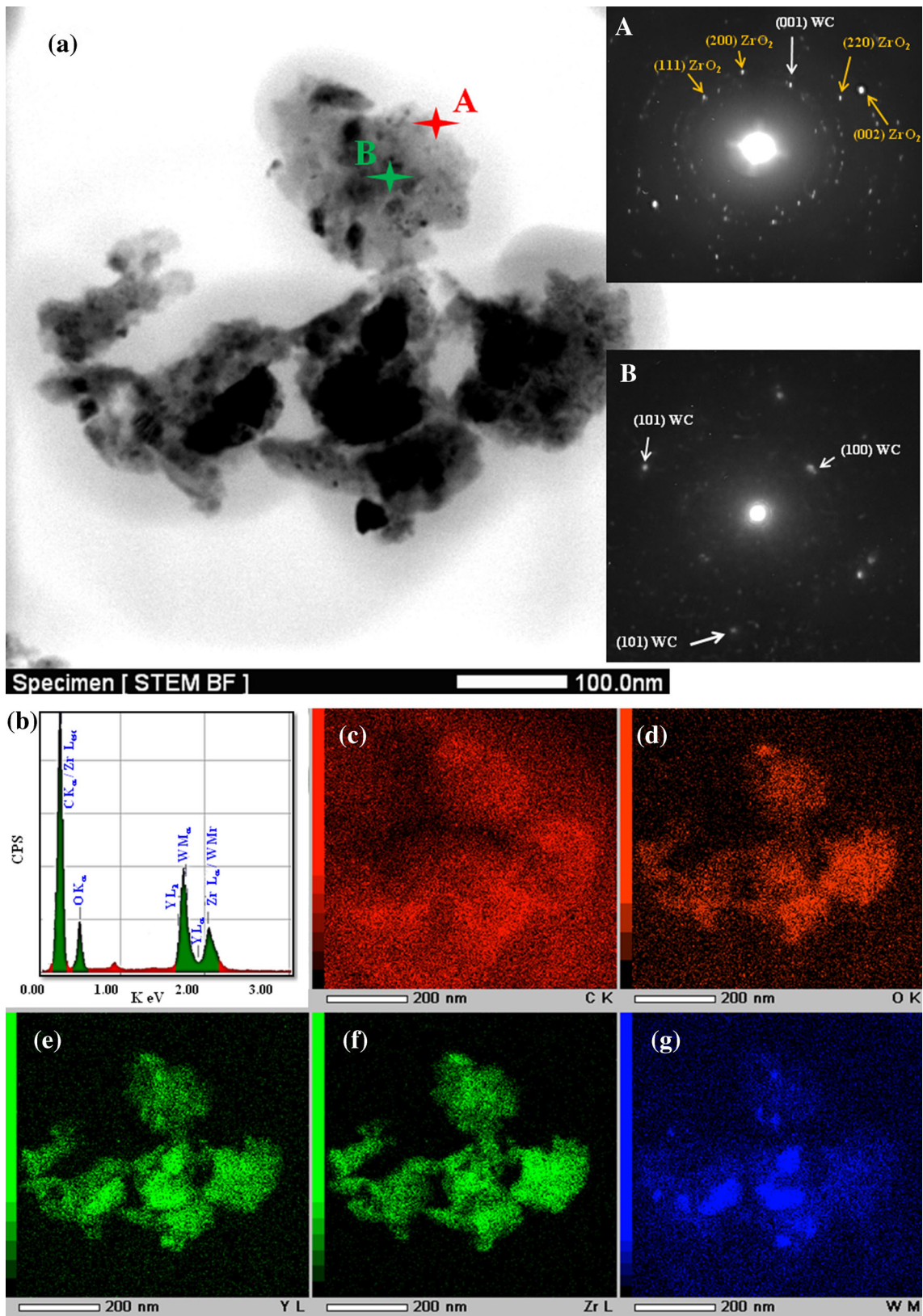


Fig. 3 (a) TEM micrograph of the N-N WC/TZ-3Y composite powder after 120-h mechanical milling; the insets show two inspected SADP for further information about the phases in the selected areas A and B. (b) The corresponding TEM-EDS mapping spectrum of the N-N WC/TZ-3Y composite after 120-h ball milling. TEM-EDS mapping of (c) C (d) O (e) Y (f) Zr and (g) W elements are presented

consolidation as the nanosized particles can be sintered at lower T_s due to the high surface-to-volume ratio that imposes increased contact points through the green compacts.

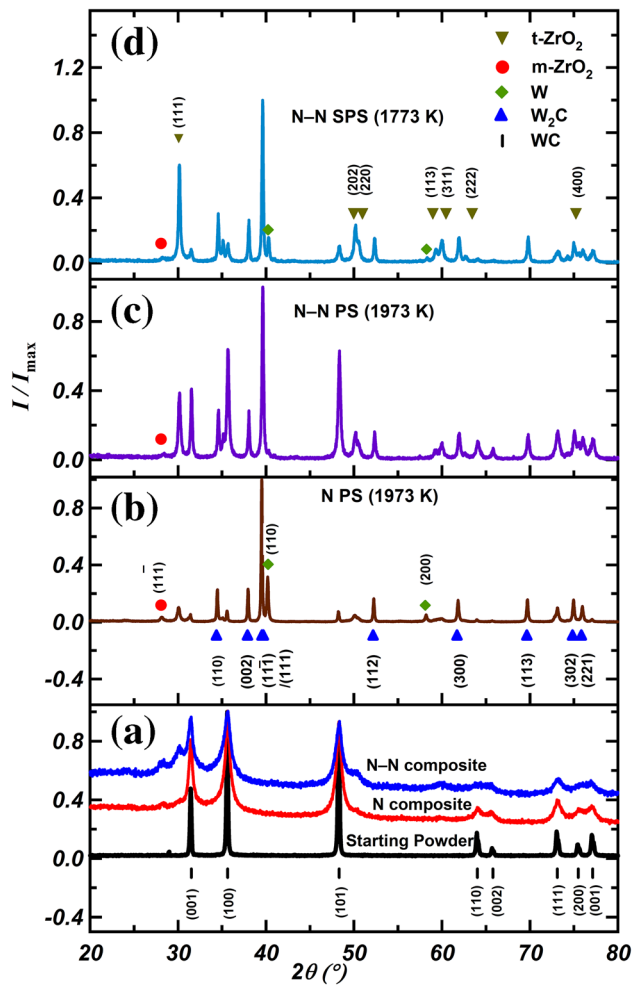


Fig. 4 Powder x-ray diffraction (PXRD) patterns of (a) a mixed WC and ZrO₂ powder before the ball milling (as prepared) and the ball-milled N and N-N composites of WC/ TZ-3Y, (b) and (c) N and N-N composites of WC/TZ-3Y after PS at 1973 K, respectively, and (d) N-N composites of WC/TZ-3Y after SPS at 1773 K

Different phases grown in the milled composites were identified by PXRD. PXRD patterns for the ball-milled powders before sintering as well as those of the as-prepared mixed powder are shown in Fig. 4(a). Indexed Bragg angles of the observed phases are indicated. No extra phases due to the excessive milling are observed in neither the N nor N-N composites. Only the hexagonal closed packed phase of WC (space group $P\bar{6}m2$, No. 187), monoclinic m-ZrO₂ (space group $P2_1/c$, No. 14) and tetragonal t-ZrO₂ (space group $P4_2m$, No. 111) are observed. It is obvious that the intensities of t-ZrO₂ peaks are little increased in the N-N composite. Interestingly, an additional peaks broadening clearly seen in the PXRD patterns of the N-N composite provides another indication, besides the TEM and HRTEM results, of the grain size reduction upon the excessive ball milling. The average crystallite size, d , for each phase can be calculated using the Scherer's equation,

$$d = \frac{0.9\lambda}{\beta \cos \theta}, \quad (\text{Eq 1})$$

where λ is the x-ray wave length, β is the full width at half maximum and θ is the diffraction Bragg angle. In consistence with HRTEM results, the average crystallite grain size estimated from PXRD using Eq 1 is less than 20 nm for both WC and TZ-3Y phases in the N-N composite. The crystallite/grain sizes of WC and TZ-3Y phases in N and N-N composites estimated from PXRD are listed in Table 2.

Figure 4(b) and (c) shows the PXRD patterns of the N and N-N WC/TZ-Y3 composites sintered by PS at 1973 K and SPS at 1773 K. It is observed that all the sintering samples exhibit major phases of W₂C (hexagonal of space group $P\bar{3}1m$ No. 162), WC (hexagonal of space group $P\bar{3}1m$ No. 162) and t-ZrO₂ (tetragonal space group $P4_2m$ No. 111). PXRD clearly indicates the growth of a new phase, W₂C, after sintering both N and N-N WC/TZ-Y3 composites at $T_s \geq 1773$ K. As well as in the milled powders, little amounts of the monoclinic phase m-ZrO₂ remain in the sintered samples. The presence of W₂C only after sintering indicates a possible reaction of WC and ZrO₂ nanoparticles at high T_s .

The formation of W₂C is reported to occur significantly by arc plasma melting and in situ casting of WC with or without W additions (Ref 24). It also grows as a minor phase by hot pressing of WC at 2423 K (Ref 28) and SPS of nanocrystalline WC at 1973 K (Ref 29). One possible source of W₂C phase

Table 2 Atomic ratios, crystallites size and lattice constants estimated from the PXRD patterns of the main phases of WC-W₂C/TZ-3Y nanocomposites based on N and N-N structures synthesized by PS and SPS techniques

Sample	Phase											
	WC (hexagonal)				W ₂ C (hexagonal)				t-ZrO ₂ (tetragonal)			
	mol.%	d_{XRD} (nm)	a (nm)	c (nm)	mol.%	d_{XRD} (nm)	a (nm)	c (nm)	mol.%	d_{XRD} (nm)	a (nm)	c (nm)
N/PS 1973 K	7.2	47	0.2897	0.2827	58.8	61.5	0.5187	0.4726	14.8	24	0.5107	0.5182
N/SPS 1773 K	2.8	50	0.2908	0.2841	52.45	49	0.5184	0.4728	27.4	28	0.5121	0.5156
N-N/PS 1973 K	36.2	29	0.2904	0.2837	27.5	43	0.5186	0.4727	34.5	28.5	0.5107	0.5187
N-N/SPS 1773 K	7.5	41	0.2904	0.2837	29.8	49	0.5186	0.4726	58.8	34	0.5106	0.5181
Standard	0.2906	0.28365 (34)	0.5190	0.4724 (35)	0.5046	0.5129 (36)

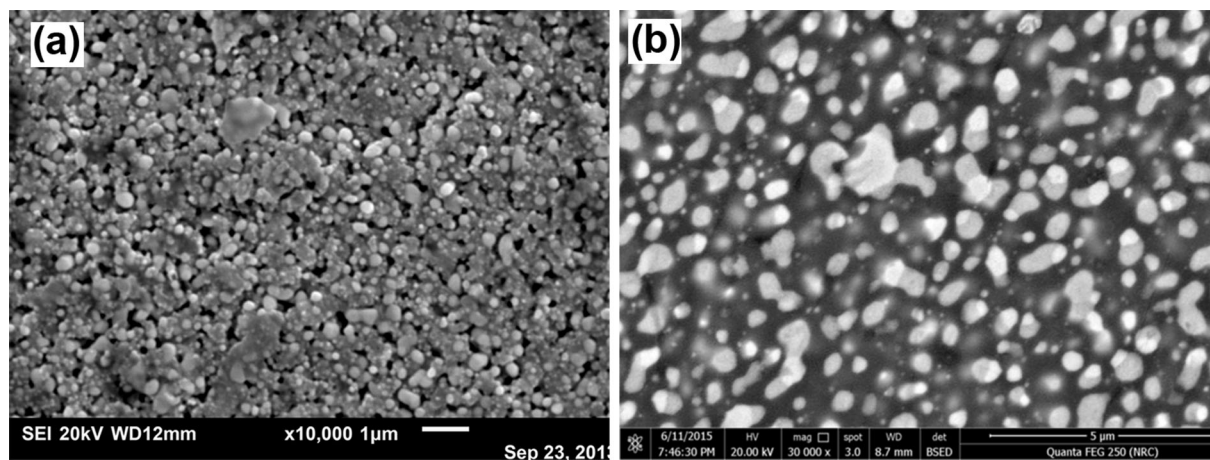
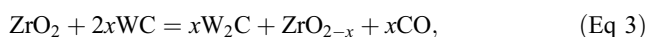


Fig. 5 SEM micrographs for (a) the N composite after PS at 1773 K showing a closed pore structure with overall porosity of $\approx 59\%$, and (b) the N-N WC/TZ-3Y composite after PS at 1773 K showing the fine microstructure and enhanced consolidation

formation is the high- T_s decarburization of the WC. With a significant carbon loss, the α -WC $_{1-x}$ phase can be formed which at high T_s leads to the formation of WC and W $_2$ C, according to the reaction (Ref 28, 29):



In previous studies of sintered WC/TZ-3Y composites, W $_2$ C phase has not been observed to grow in the case of bulk WC crystallites, for instance, PS sintering at 1773-1973 K for 1 h (Ref 30) and SPS at 1573 K without holding time at sintering T (Ref 9) or at 1473-1673 K for 5 min (Ref 17). However, it was observed that WC with binder of TZ-3Y nanocrystals, mixed by WC ball milling for 24 h, results in W $_2$ C phase growth in the samples SPS-sintered at $T_s \geq 1773$ K with holding time ≥ 5 min (Ref 22). From these previous reports, the growth of W $_2$ C in sintered WC/TZ-3Y composites is influenced by the sintering conditions and the crystallite size of the starting constituents. The contribution of ZrO $_2$ in the occurrence of W $_2$ C phase can be attributed to a possible reaction between ZrO $_2$ and WC (Ref 22):



where x is the additional oxygen vacancies concentration created in the ZrO $_2$ due to this reaction. The nanoscale of ZrO $_2$, WC or both increases the reaction probability which contributes in the formation of W $_2$ C phase in large amounts.

On the other hand, a possible composition/dissociation reaction is reported to take place in WC composites at 1523-1573 K (Ref 31):



cannot be ruled out in the sintering process and provides an explanation for the W by-product and the varied WC content observed in the PXRD patterns shown in Fig. 4(b) and (c). This mechanism may be enhanced by the reduced particle size of WC and the higher T_s resulting in little decrease in the W $_2$ C phase content. Actually, the PXRD patterns indicate that starting with WC coarse particles and fine nanoparticles of the binder ZrO $_2$ results in large phase transformation of WC to W $_2$ C after sintering, i.e., W $_2$ C content is higher in N composites, while WC increases in N-N composites, as pre-

sented in Table 2. The relative atomic ratios of the formed phases are estimated from the area under the PXRD peaks of each phase. We attribute the graded W $_2$ C content from higher in the N structure to lower in N-N-structured composites to a competing formation and dissociation mechanisms of W $_2$ C as the particle size of WC is reduced. The crystallite sizes of the resultant phases, presented in Table 2, were estimated from the observed PXRD patterns using Eq 1. It can be seen that the grains of the starting phases and W $_2$ C phase are maintained on nanoscale after sintering. Grains aggregation has been reported to occur for nanocrystalline metal oxides after sintering (Ref 32), which explains the increased grain size of zirconium oxide in the sintered N and N-N nanocomposites. The lattice constants estimated from the PXRD patterns of the main phases in the PS- and SPS-sintered samples are also included in Table 2. Reported values of lattice constants are presented for comparison.

3.2 Microstructure and Densification

Based on density measurements using Archimedes' principle, which are listed in Table 2, pellets of N composite PS-sintered at 1773 K showed insufficient consolidation (59% of the theoretical density, TD), while the pellets of N-N composite were consolidated up to 88% TD using the same conditions. In fact, SPS at 1773 K or even PS at higher T_s enhances the consolidation. It is worth mentioning that the theoretical density was calculated by employing the rule of mixtures taking into account that the theoretical density of WC is 15.63 g/cm 3 and that of TZ-3Y is 5.64 g/cm 3 (Ref 33). The measured density values listed in Table 2 were further confirmed by porosity analysis for the well-polished sintered samples by making use of the SEM images and employing the Image-J software. Knowing the relative density, f_s , of the sintered specimen and the green compact relative density, f_g , the densification parameter ψ can be calculated by the relation (Ref 21),

$$\psi = \frac{(f_s - f_g)}{(1 - f_g)}. \quad (\text{Eq 5})$$

In comparison, values of ψ of similar composites with relatively coarse grains size were reported in ranges of 26-42%

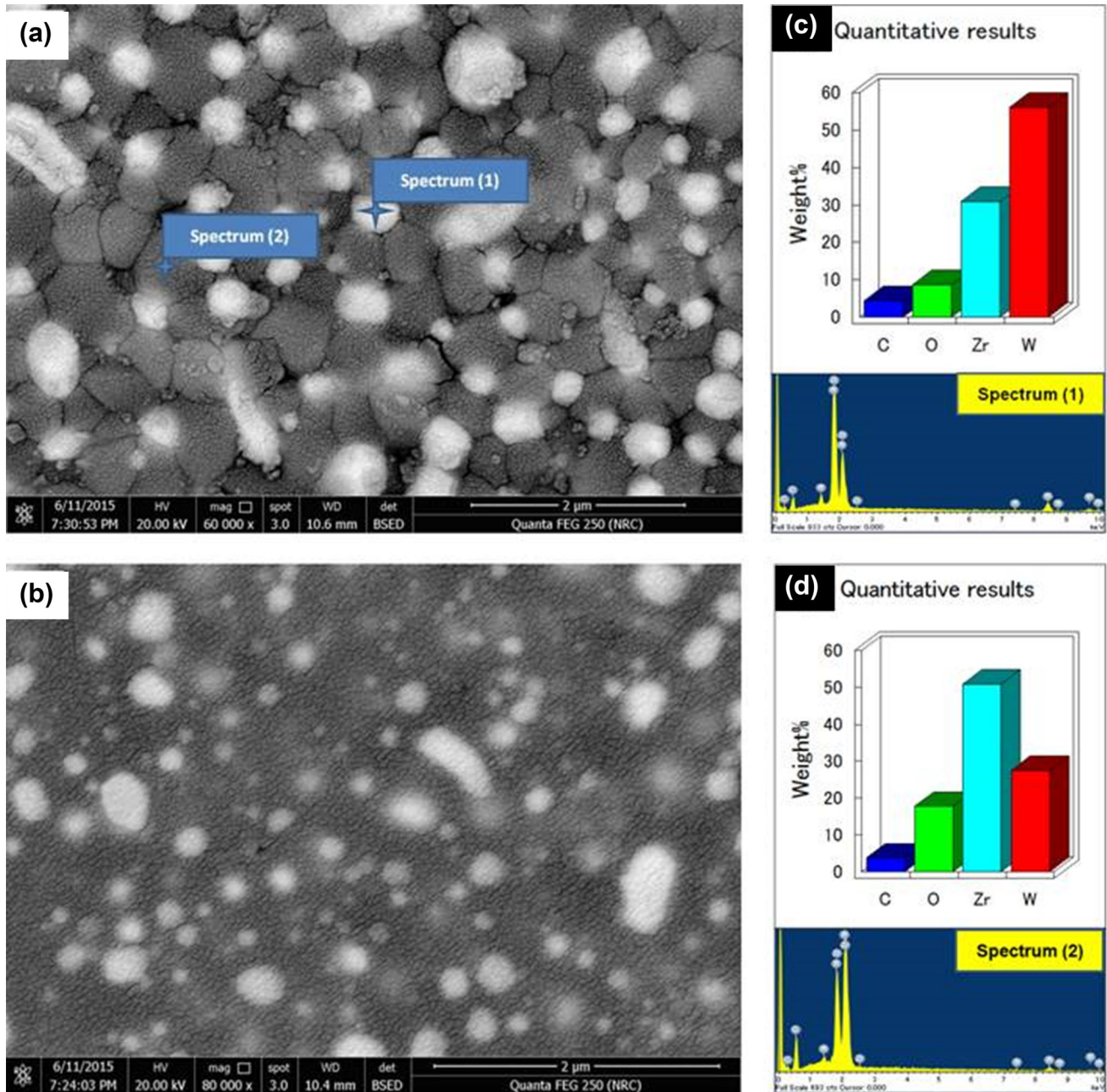


Fig. 6 SEM images for (a) N composite after PS at 773 K and (b) N-N composite after PS at 773 K. SEM for N-N shows high consolidated structure with less pores and finer structure. SEM-EDS analysis for (c) the gray and (d) the white areas in the microstructure of N and N-N sintered specimens

(Ref 17, 22). Higher values of ψ are expected with reduced grains size, for instance, ψ for our N-N composite PS-sintered at 1773 K is about 84%. The relatively high ψ in the current study reveals the potential for the N-N composite to be sintered to high density at this low T_s if the green compact relative density could be further enhanced, for example, by cold isostatic pressing.

Figure 5(a) and (b) shows SEM micrographs for the N and N-N composites, respectively, when PS-sintered at 1773 K. The porous structure of the sintered pellet of N composite (Fig. 5a) explains the previously mentioned low density of this composite. The pores almost disappeared for the finer particles pellet (N-N) sintered at the same T_s

(Fig. 5b). The porous structure of N composite may be of interest for next studies include impregnation with liquid or soft metal. SEM micrograph in Fig. 6(a) shows that the consolidation level of the N composite is scaled up when the PS is performed at 1973 K. Much higher consolidation level with finer structure appears in the SEM micrograph of the N-N composite sintered at 1973 K, as shown in Fig. 6(b). It is clear now that the increase in surface-to-volume ratio of the N-N composite directly contributes to the enhanced densification. The gray areas appear in the SEM micrographs are areas rich of ZrO_2 more than WC and W_2C phases, while in opposite, the white islands are areas of lower concentrations of ZrO_2 as indicated by the SEM-EDS point analysis

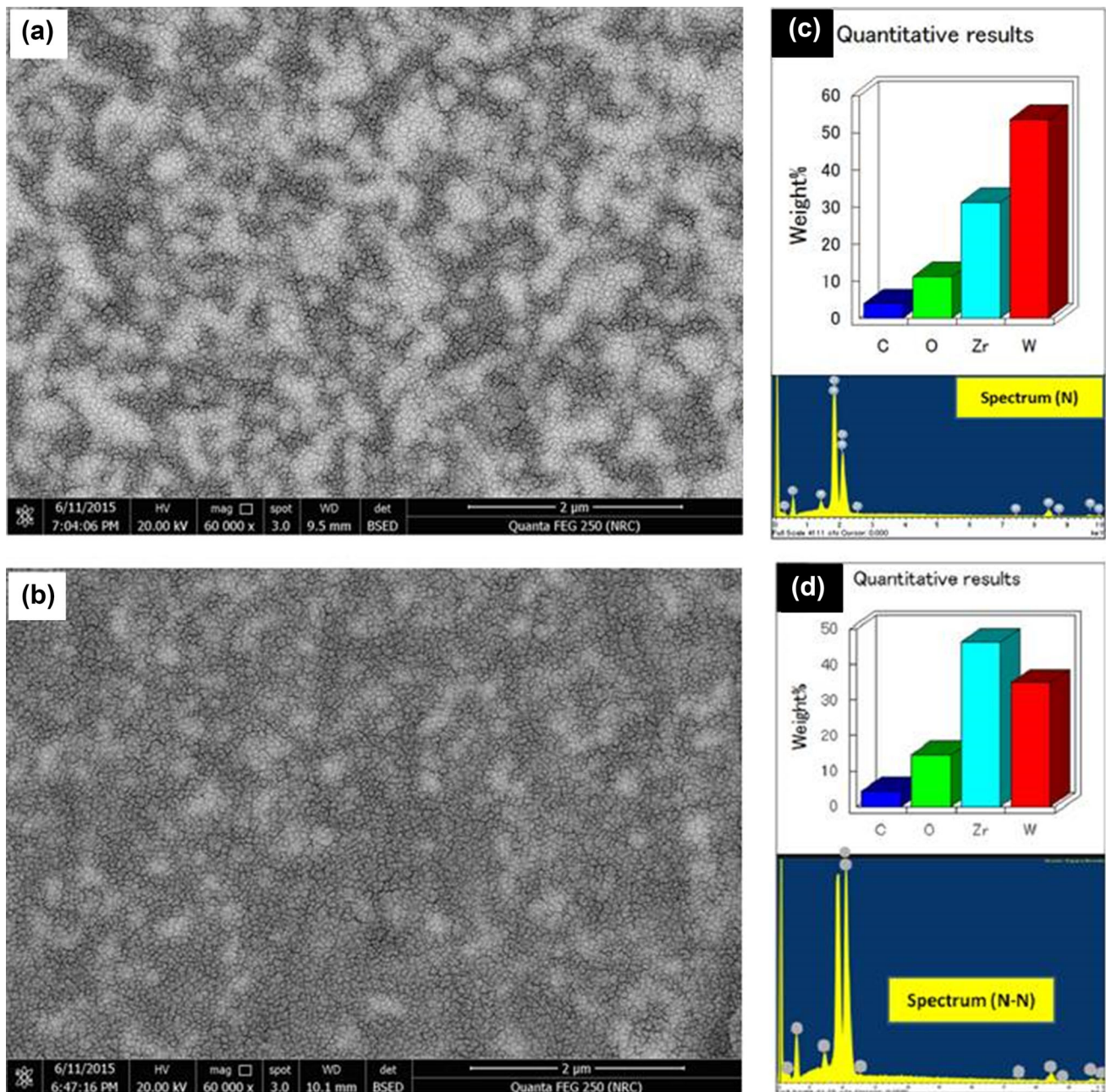


Fig. 7 SEM micrographs of (a) the N composite and (b) N-N composite of WC/TZ-3Y after SPS at 1773 K showing a high consolidated structure. (c) and (d) SEM-EDS mapping spectrum for N and N-N SPS-sintered specimens, respectively

shown in Fig. 6(c) and (d) for the gray and white areas, respectively.

As mentioned above, the remaining porosity in the sintered specimens is often due to the lack of green compact density, which retards the sintering kinetics and sintering mechanisms. This claim is supported by the SPS results at the lower T_S (1773 K), whereas the high green density is not a precondition for a good consolidation (Ref 18, 19). Density results for both N and N-N composites were in the range of 96-98% TD, very close to the theoretical values as indicated by measurements based on Archimedes' principal as well as the porosity analysis inspections. The microstructures, SEM micrographs, of the SPS-sintered specimens are shown in Fig. 7(a) and (b) for N

and N-N composites, respectively. The refined particle size is maintained due to the short time of SPS. Area mapping with EDS for SPS-sintered N and N-N specimens in Fig. 7(c) and (d), respectively, shows again the higher average ZrO_2 content in N-N composite, ~45%, than in N composite, ~30%.

3.3 Mechanical Properties

In addition to other factors such as the consolidation level, the Vicker microhardness and nanoindentation techniques indicate significant enhancements of the mechanical properties for the developed WC-W₂C/TZ-3Y composites by the increased W₂C content. Figure 8 shows the measured micro-

hardness values for the PS- and SPS-sintered N and N-N composites. To report reliable values of the measured microhardness, ten randomly measured readings on the surface of well-polished specimens were considered in the average microhardness calculation. The PS results in large variation in the hardness from 1.37 to 15.70 GPa for the N structure composites when sintered at 1773 and 1973 K, respectively, while the N-N composites show little enhancement in the microhardness from 14.61 to 14.71 GPa with increasing T_s from 1773 to 1973 K, respectively. However, the error bar of the sample N-N/PS-sintered at 1973 K indicates a tendency to higher microhardness. There was an increase in the hardness of the sufficiently consolidated N composite, 15.70 GPa, compared to the hardness of the N-N composite, 14.71 GPa, at the same PS temperature (1973 K).

SPS at 1773 K well enhances the microhardness of N composite, 18.29 GPa, and almost results in the same value resulted by the PS for the fine particle N-N composite as shown in Fig. 8 and Table 3. The slight decrease in the microhardness of N-N compared to N composite after PS at 1973 K or SPS at 1773 K is mainly attributed to the higher W_2C content in the sintered N composites, resulting in the fused WC- W_2C /TZ-3Y composite, as in Table 2. Furthermore, the increased ZrO_2

content in the N-N composites indicated by PXRD results in Table 2 and SEM-EDS results in Fig. 6 and 7 may add little softness to the sintered composite (Ref 13). SPS-sintered N composites show the highest microhardness values, which is attributed to the higher density, higher grown W_2C content and the lower ZrO_2 content.

Nanoindentation test performed for sintered N-N composites of fine particles indicates high modulus of elasticity. Figure 9 shows the load-displacement curves of the N-N composite PS- and SPS-sintered at 1973 and 1773 K, respectively. Moreover, with ignoring the effect of pores on the nanoscale, the hardness of a material can be calculated based on the nanoindentation technique using the permanent displacement reading. The average of eight readings reveals high values of the modulus of elasticity as well as the nanoscale hardness of N-N sintered composite. The nanoscale hardness is much enhanced by SPS to 25.34 GPa or even by PS sintering at 1973 K, 22.33 GPa. The values of Young's modulus and the calculated hardness obtained from nanoindentation are listed in Table 2. The discrepancy in the values of nanoscale hardness obtained by nanoindentation and the measured microhardness may be due to the effects of remaining pores in the microstructure of the sintered samples. Our results indicate the success of the

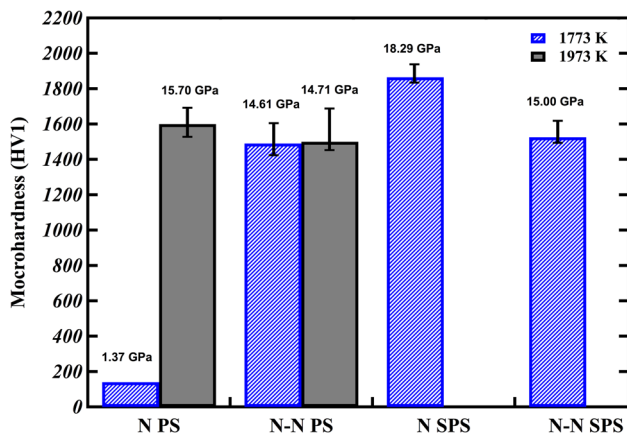


Fig. 8 Microhardness data for the N and N-N WC/TZ-3Y composites, PS-sintered at 1773 and 1973 K and SPS-sintered at 1773 K. Error bars are shown and relatively small for N composite PS-sintered at 1773 K

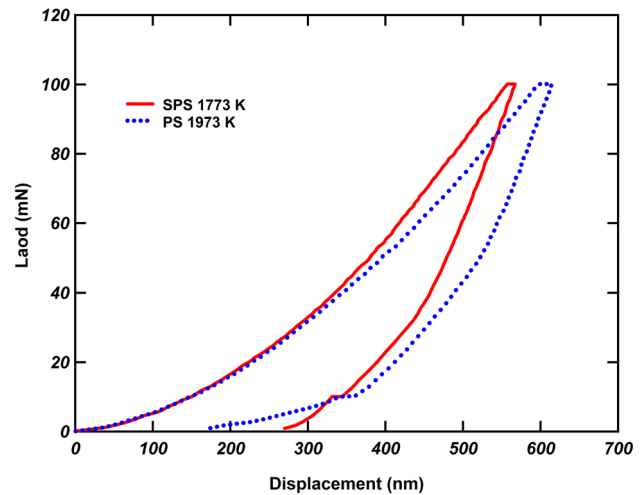


Fig. 9 Load-displacement curves of nanoindentation test for the N-N WC/TZ-3Y composite after a PS at 1973 K and SPS at 1773 K

Table 3 Observed mechanical properties of WC- W_2C /TZ-3Y nanocomposites based on N and N-N structures synthesized by PS and SPS techniques at indicated temperatures

Sample/sintering conditions	Relative density, % TD	Microhardness, GPa	Nanoscale hardness, GPa	Young's modulus, GPa
N/PS 1773 K	59	1.37
N/PS 1973 K	96	15.70
N/SPS 1773 K	97	18.29
N-N/PS 1773 K	88	14.61	20.10	322
N-N/PS 1973 K	98	14.71	22.33	340
N-N/SPS 1773 K	99	15.00	25.34	560

presented processing in obtaining ceramics of the fused tungsten carbide/zirconia, WC-W₂C/TZ-3Y, of high hardness fits the cutting tools functions.

4. Conclusion

Mechanical ball milling can be employed to make a good refinement for the hard tungsten carbide and ZrO₂-3 mol.% Y₂O₃ powders down to the nanometer scale. For instance, ball milling for 120 h results in WC/TZ-3Y nano-nano (N-N) composites of grain sizes of WC and TZ-3Y in the order of 10 nm as indicated by HRTEM observations and PXRD measurements. PXRD and SEM-EDS analysis revealed the phase transformation of WC to W₂C resulting in the fused tungsten carbide/zirconia, WC-W₂C/TZ-3Y, in both N- and N-N-structured composites when sintered at $T_s \geq 1773$ K. As well as SPS technique and the conventional pressure-less sintering (PS) technique can be employed to produce dense and hard WC-W₂C/TZ-3Y composites, as indicated Vicker microhardness and nanoindentation measurements. Except for the little consolidated samples by PS at 1773 K, composites based on the N structure which exhibit higher W₂C content showed higher microhardness than those for N-N structure containing less W₂C. For instance, after SPS at 1773 K, the N-based structure showed a microhardness of 18.24 GPa against 15 GPa for the N-N-based structure. Based on nanoindentation results, modulus of elasticity up to 340 and 560 GPa and hardness up to 22.33 and 25.34 GPa can be realized for the N-N-structured WC-W₂C/ZrO₂ nanocomposites obtained by PS at 1773 K and by SPS at 1773 K, respectively.

Acknowledgment

This work is supported by Egypt-Japan University of Science and Technology (EJUST). The authors are grateful to Prof. H. Nakamura from the Department of Material Science and Engineering, Kyoto University, for his support in samples preparation and characterization. Prof. K. Shinagawa and Prof. Y. Tanaka from the Faculty of Engineering, Kagawa University, are acknowledged for electron diffraction facilities and fruitful discussion in the microstructure analysis. M.A.K. and A.N. would like to thank the Ministry of Higher Education (MOHE) of Egypt for the financial support during their study.

References

1. D. Whitney, Ceramic Cutting Tools, *Comprehensive Hard Materials*, 1st ed., V. Sarin, Ed., Elsevier, New York, 2014, p 491–505
2. S. Dolinšek, B. Šuštaršič, and J. Kopač, Wear Mechanisms of Cutting Tools in High-Speed Cutting Processes, *Wear*, 2001, **250**, p 349–356
3. X.S. Li and I.M. Low, Ceramic Cutting Tools—An Introduction, *Key Eng. Mater.*, 1994, **96**, p 1–18
4. M.S. El-Eskandarany, A.A. Mahday, H.H.A. Ahmed, and A.H. Amer, Synthesis and Characterizations of Ball-Milled Nanocrystalline WC and Nanocomposite WC-Co Powders and Subsequent Consolidations, *J. Alloys Compd.*, 2000, **312**, p 315–325
5. R.W. Armstrong, The Hardness and Strength Properties of WC-Co Composites, *Materials (Basel)*, 2011, **4**, p 1287–1308
6. Z. Fang, P. Maheshwari, X. Wang, H.Y. Sohn, A. Griffo, and R. Riley, An Experimental Study of the Sintering of Nanocrystalline WC-Co Powders, *Int. J. Refract. Met. Hard Mater.*, 2005, **23**, p 249–257
7. M.S. El-Eskandarany, H.M.A. Soliman, and M. Omoric, Influence of Nanocrystalline ZrO₂ Additives on the Fracture Toughness and Hardness of Spark Plasma Activated Sintered WC/ZrO₂ Nanocomposites Obtained by Mechanical Mixing Method, *Open J. Compos. Mater.*, 2012, **02**, p 1–7
8. I.-J. Shon, I.-K. Jeong, I.-Y. Ko, J.-M. Doh, and K.-D. Woo, Sintering Behavior and Mechanical Properties of WC-10Co, WC-10Ni and WC-10Fe Hard Materials Produced by High-Frequency Induction Heated Sintering, *Ceram. Int.*, 2009, **35**, p 339–344
9. A. Mukhopadhyay, D. Chakravarty, and B. Basu, Spark Plasma-Sintered WC-ZrO₂-Co Nanocomposites with High Fracture Toughness and Strength, *J. Am. Ceram. Soc.*, 2010, **93**, p 1754–1763
10. J. Ma, S.G. Zhu, P. Di, and Y. Zhang, Influence of La₂O₃ Addition on Hardness, Flexural Strength and Microstructure of Hot-Pressing Sintered WC-MgO Bulk Composites, *Mater. Des.*, 2011, **32**, p 2125–2129
11. H. Qu, S. Zhu, Q. Li, and C. Ouyang, Influence of Sintering Temperature and Holding Time on the Densification, Phase Transformation, Microstructure and Properties of Hot Pressing WC-40 vol.%Al₂O₃ composites, *Ceram. Int.*, 2012, **38**, p 1371–1380
12. S. Imasato, K. Tokumoto, T. Kitada, and S. Sakaguchi, Properties of Ultra-fine Grain Binderless Cemented Carbide “RCCFN”, *Int. J. Refract. Met. Hard Mater.*, 1995, **13**, p 305–312
13. O. Malek, B. Lauwers, Y. Perez, P. De Baets, and J. Vleugels, Processing of Ultrafine ZrO₂ Toughened WC Composites, *J. Eur. Ceram. Soc.*, 2009, **29**, p 3371–3378
14. G. Anné, S. Put, K. Vanmeensel, D. Jiang, J. Vleugels, and O. Van der Biest, Hard, Tough and Strong ZrO₂-WC Composites from Nanosized Powders, *J. Eur. Ceram. Soc.*, 2005, **25**, p 55–63
15. B. Basu, T. Venkateswaran, and D. Sarkar, Pressureless sintering and tribological properties of WC-ZrO₂ composites, *J. Eur. Ceram. Soc.*, 2005, **25**, p 1603–1610
16. B. Basu and K. Balani, *Advanced Structural Ceramics*, Wiley, New Jersey, 2011
17. B. Basu, J.-H. Lee, and D.-Y. Kim, Development of WC-ZrO₂ Nanocomposites by Spark Plasma Sintering, *J. Am. Ceram. Soc.*, 2004, **87**, p 317–319
18. B. Wang, K. Matsumaru, J. Yang, Z. Fu, and K. Ishizaki, The Effect of cBN Additions on Densification, Microstructure and Properties of WC-Co Composites by Pulse Electric Current Sintering, *J. Am. Ceram. Soc.*, 2012, **95**, p 2499–2503
19. B. Wang, Y. Qin, F. Jin, J.-F. Yang, and K. Ishizaki, Pulse Electric Current Sintering of Cubic Boron Nitride/Tungsten Carbide-cobalt (cBN/WC-Co) Composites: Effect of cBN Particle Size and Volume Fraction on Their Microstructure and Properties, *Mater. Sci. Eng. A*, 2014, **607**, p 490–497
20. O. Eso, Z. Fang, and A. Griffo, Liquid Phase Sintering of Functionally Graded WC-Co Composites, *Int. J. Refract. Met. Hard Mater.*, 2005, **23**, p 233–241
21. R.M. German, *Sintering Theory and Practice*, Wiley, New York, 1996
22. K. Biswas, A. Mukhopadhyay, B. Basu, and K. Chattopadhyay, Densification and Microstructure Development in Spark Plasma Sintered WC-6 wt.% ZrO₂ Nanocomposites, *J. Mater. Res.*, 2007, **22**, p 1491–1501
23. A.S. Kurlov and A.I. Gusev, Tungsten Carbides and W-C Phase Diagram, *Inorg. Mater.*, 2006, **42**, p 121–127
24. T. Dash and B.B. Nayak, Preparation of WC-W₂C Composites by Arc Plasma Melting and Their Characterisations, *Ceram. Int.*, 2013, **39**, p 3279–3292
25. H.S.W. Yih and C.T. Wang, *Tungsten Sources, Metallurgy and Applications*, Plenum Press, New York, 1981
26. W.-T. Chen, C.H. Meredith, and E.C. Dickey, Growth and Microstructure-Dependent Hardness of Directionally Solidified WC-W₂C Eutectoid Ceramics, *J. Am. Ceram. Soc.*, 2015, **98**, p 2191–2196
27. K. Niihara, New Design Concept of Structural Ceramics-Ceramic New Design Concept of Structural Ceramics-Ceramic Nanocomposites, *J. Ceram. Soc. Jpn.*, 1991, **99**, p 974–982
28. A. Gubernat, P. Rutkowski, G. Grabowski, and D. Zientara, Hot Pressing of Tungsten Carbide with and Without Sintering Additives, *Int. J. Refract. Met. Hard Mater.*, 2014, **43**, p 193–199
29. M. Dopita, C. Sriram, Spark Plasma Sintering of Nanocrystalline Binderless WC Hard Metals, *Proceedings of the Conference on Nanocon, Olomouc, Czech Repub*, 2010, p 10–15

30. B. Basu, J.H. Lee, and D.Y. Kim, Processing of Nanoceramics and Nanoceramic Composites: New Results, *Key Eng. Mater.*, 2004, **264-268**, p 2293–2296
31. V.Z. Kublii, T.Y. Velikanova, O.A. Gnitetskii, and S.I. Makhovitskaya, Structural Parameters of the Low-Temperature Metastable form of the Carbide W_2C , *Powder Metall. Met. Ceram.*, 2000, **39**, p 151–156
32. S.A. Makhlouf, M.A. Kassem, and M.A. Abdel-Rahim, Particle Size-Dependent Electrical Properties of Nanocrystalline NiO, *J. Mater. Sci.*, 2009, **44**, p 3438–3444
33. M.J. Pascual, A. Durán, and L. Pascual, Sintering Behaviour of Composite Materials Borosilicate Glass-ZrO₂ Fibre Composite Materials, *J. Eur. Ceram. Soc.*, 2002, **22**, p 1513–1524
34. A.D. Krawitz, D.G. Reichel, and R. Hitterman, Thermal Expansion of Tungsten Carbide at Low Temperature, *J. Am. Ceram. Soc.*, 1989, **72**, p 515–517
35. T. Epicier, J. Dubois, C. Esnouf, G. Fantozzi, and P. Convert, Neutron Powder Diffraction Studies of Transition Metal Hemicarbides M_2C_{1-x} —II. In Situ High Temperature Study on W_2C_{1-x} and Mo_2C_{1-x} , *Acta Metall.*, 1988, **36**, p 1903–1921
36. L.C. Ming, J.B. Balogh, S. Qadri, E.F. Skelton, D. Schiferl, and M.H. Manghnani, Equation of State and Phase Transition Studies Under In Situ High P-T Conditions Using Synchrotron Radiation, Reidel, Boston MA, *Solid State Physics under Pressure: Recent Advance with Anvil Devices*, S. Minomura, Ed., Terra Scientific Publishing, Tokyo, 1985, p 343–350